JACS
JOURNAL OF THE AMERICAN CHEMICAL SOCIETY
pubs.acs.org/JACS
Article

Diffusion-Mediated Nucleation and Growth of fcc and bcc Nanocrystal Superlattices with Designable Assembly of Freestanding 3D Supercrystals

Xin Huang, Elizabeth Suit, Jinlong Zhu, Binghui Ge, Frauke Gerdes, Christian Klinke, and Zhongwu Wang*

Cite This: *J. Am. Chem. Soc.* 2023, 145, 4500−4507

Read Online

ACCESS | Metrics & More | Article Recommendations | Supporting Information

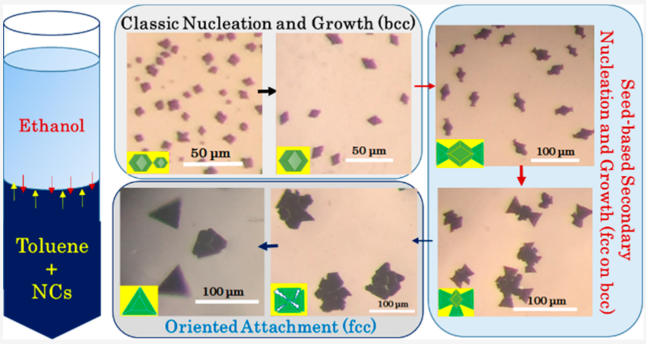

ABSTRACT: Diffusion-mediated assembly of octahedral PbS nanocrystals (NCs) in a confined antisolvent environment displays a primary burst nucleation and Ostwald ripening growth of rhombic bcc supercrystals, followed by a secondary seed-based nucleation and oriented attachment growth of triangle fcc supercrystals. As the diffusion proceeds from ethanol across a sharp interface into NC-suspended toluene, a burst nucleation of supercrystal seeds occurs, and such supercrystals are quickly developed into rhombic grains that have a bcc structure. At a critical size of 10 μm, an Ostwald ripening event appears to guide the supercrystal growth. Upon grain growth above 30 μm, the fcc supercrystals start a nucleation at two symmetrical tips of individual rhombic crystals. Such fcc supercrystals are developed with a triangle shape, and two triangles are combined with one bcc rhombus in-between to form a butterfly-like bowtie stacking structure. The fcc triangle wings grow larger at a reduction of bcc rhombus cores. As the bcc cores gradually fade, such butterfly-like bowtie crystals aggregate and undergo an oriented attachment process, leading to the formation of freestanding 3D triangle crystals that have a single fcc lattice. Analysis of experimental observations and defined diffusion parameters reveals that fast solvent diffusion and high-NC concentration promote the growth of rhombic bcc supercrystals, while slow solvent diffusion and low-NC concentration accelerate the development of triangle fcc supercrystals. Upon succeeding in designable growth of 3D fcc supercrystals, this study provides designing principles for controlled fabrication of supercrystals with desired superlattices for additional engineering and applications.

INTRODUCTION

Colloidal nanocrystals (NCs), which serve as designable atoms, can spontaneously self-assemble into periodically ordered superlattices.[1−3] Such superlattice solids, called "designer solids", represent completely the new category of condensed matters, which not only can be used to explore the newly emergent properties at mesoscale[4,5] but also can be engineered into higher hierarchical materials.[6−9] Upon discovery of collective properties from a variety of NC assembles, recent pressure engineering of such NC-ordering supercrystals has enabled 100% retention of high pressure metastable phases at ambient conditions.[10] Such single NC supercrystals also display noticeable anisotropy of collective property as superlattices change in space symmetry and crystallographic orientation.[11−14] In order to make better use of such unique properties and further enable fine-tuning and controllable engineering of such supercrystals, it is crucial to explore and find ways of designable control of NC assembly environments to grow large free-standing 3D single supercrystals with desired superlattices.

Previous studies have revealed the complexity of the crystal nucleation and growth in nanocrystals and biological and geological materials,[15−24] which involves a burst nucleation of small seed crystals at the very early stage[15−17] and subsequently a complex growth of seed crystals in terms of multiple interactions of Ostwald ripening, oriented attachment, and other components.[18−24] In a 2D NC assembly such as thin film, it is observed that colloidal NCs undergo a crystallization and growth process similar to what atoms do,[24−26] but unfortunately, how 3D supercrystals nucleate and grow in a free-standing way from NC suspensions in solvents still remains largely unknown.

Received: October 19, 2022
Published: February 14, 2023

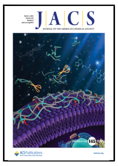

ACS Publications

https://doi.org/10.1021/jacs.2c11120

The nucleation of 3D atomic crystals is considered as a saturation-induced consequence of dissolved ions under a solution environment,[15−17,24] so we employed octahedral PbS NCs as an example and designed an antisolvent diffusion cell to modify NC solubility and control NC concentration. As a result, such a diffusion-mediated process not only was able to spontaneously trigger the nucleation and growth of NC assembly into 3D free-standing supercrystals but also could enable an effective modification of superlattice symmetry and gradual development of supercrystal shape. Utilizing synchrotron-based X-ray scans and direct visualization under microscopy as well as electron microscopic imaging, we were able to map out the distributions of structure, grain size, and shape of NC supercrystals across the whole glass capillary. These observations and characterizations were subsequently correlated to the observed time-dependent antisolvent diffusion rate, capable of an overall understanding of the diffusion-mediated nucleation and growth of 3D supercrystals and underlying mechanisms. With such experiments and defined parameters as well as collected insights, we stepped a bit further and designed additional control experiments and truly achieved designable growth of 3D free-standing fcc supercrystals, which were rarely observed in self-assemblies of octahedral NCs made up of various compositions.[26−29]

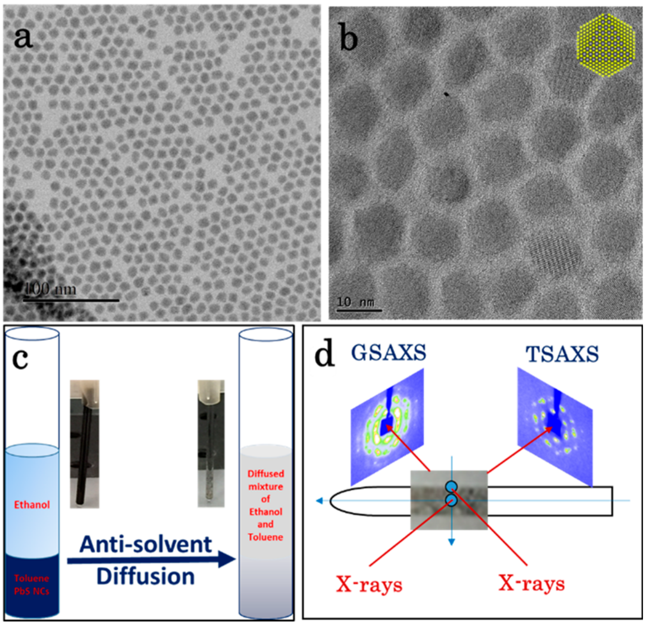

Figure 1. Characterizations and self-assembly setup of octahedral PbS NCs: (a, b) typical low and high resolution TEM images of as-synthesized PbS NCs with an octahedral shape; (c) diffusion-mediated self-assembly setup of octahedral PbS NCs under a confined antisolvent environment, where ethanol is directly overlaid on the top of toluene to form a soft and sharp interface; (d) synchrotron-based SAXS scans of NC assemblies across the long (e.g., horizontal blue line) and cross-section (e.g., vertical blue line) directions of the capillary. Note that GSAXS and TSAXS in (c) represent the grazing-incidence-like and transmission SAXS, respectively, in which the incident X-rays are footprinted typically on the central and edge spots of the capillary across the cross section, respectively, as highlighted by the two solid circles in blue.

■ RESULTS AND DISCUSSION

PbS NCs were synthesized using a literature-reported protocol with a slight modification.[30] The same batch of NCs used in previous in situ 2D assembly[26] were used in this 3D NC assembly study as well. Synchrotron-based X-ray scattering inspection at a wide angle range reveals that PbS NCs have an atomic fcc structure ($Fm3m$) with a cell constant of a = 5.936 Å (Figure S1). Transmission electron microscopy (TEM) characterizes that PbS NCs are homogeneous and have an octahedral shape with an edge length of 10.5 nm (Figures 1a,b and S2; also see ref 26). In situ 2D assembly experiments of such octahedral NCs revealed a phase transformation from a face-centered cubic (fcc) to a body-centered cubic (bcc) superlattice, but only a bcc superlattice was finally harvested,[26] consistent with the drop-casting experiments (Figure S3) and previous studies on various compositions of octahedral NCs, including PbS, Pt_3Ni, and Pt_3Cu_2 NCs.[26−29] In essence, these experiments are performed as a series of 2D NC assembles, which mostly involve an interface-driven kinetic process (e.g., air/liquid, substrate/liquid). They are significantly different from the crystallization of free-standing 3D NC supercrystals in solvent due to a spontaneously triggered NC saturation under a thermodynamic equilibrium.[31−34]

In order to control NC concentration and NC solubility with an ability to trigger a spontaneous nucleation and subsequent growth of free-standing 3D supercrystals from NC-suspensions, we designed and fabricated a typical antisolvent diffusion-mediated experiment (Figure 1c), in which ethanol and NC-suspended toluene with a volumetric ratio of 2:1 were confined in a vertically oriented glass capillary to form a soft and sharp liquid/liquid interface (Figure 1c and Figure S4, left), where the starting NC concentration in toluene was 10 mg/mL. Upon gradual diffusion of ethanol into toluene, NC solubility was reduced, and accordingly NC concentration spontaneously increased. Once a NC saturation was achieved in the diffused range of antisolvents, 3D supercrystals started to nucleate and gradually grow larger (Figure S4, middle). As the diffusion process continued, 3D supercrystals formed at various stages were distributed at the corresponding wall locations of the glass capillary. Clarity and homogeneity of the diffused antisolvents were indicative of the completeness of the antisolvent diffusion and NC assembly process (Figure S4, right). As the whole process was accomplished, the solvents were immediately dumped out. Then, the supercrystals distributed on the capillary wall were scanned by synchrotron-based SAXS (Figure 1d) and visualized under optical and electron microscopes.

Synchrotron-based SAXS scans were made on the central spot of each cross section of the capillary, which started from the interface and ended at the bottom of the capillary (Figure 1d, horizontal line in blue). In this transmission geometry, incident X-rays were normal to the wall surfaces and penetrated through the glass wall into attached supercrystals. The collected transmission SAXS, called TSAXS, provided significant in-plane structural information on supercrystals. Upon a primary examination of supercrystal structures, additional SAXS scans were made across several typical cross sections located at the defined distances from the interface of the capillary (Figure 1d, vertical line in blue). In this cross-section SAXS scan, incident X-rays were tangentially footprinted on the supercrystals at the capillary edge. Correspondingly, the collected SAXS images were similar to the grazing-incidence-like SAXS, called GSAXS, and provided critical out-of-plane information on supercrystals. TSAXS and GSAXS were combined to include both in-plane and out-of-plane structural information, allowing one to unambiguously resolve

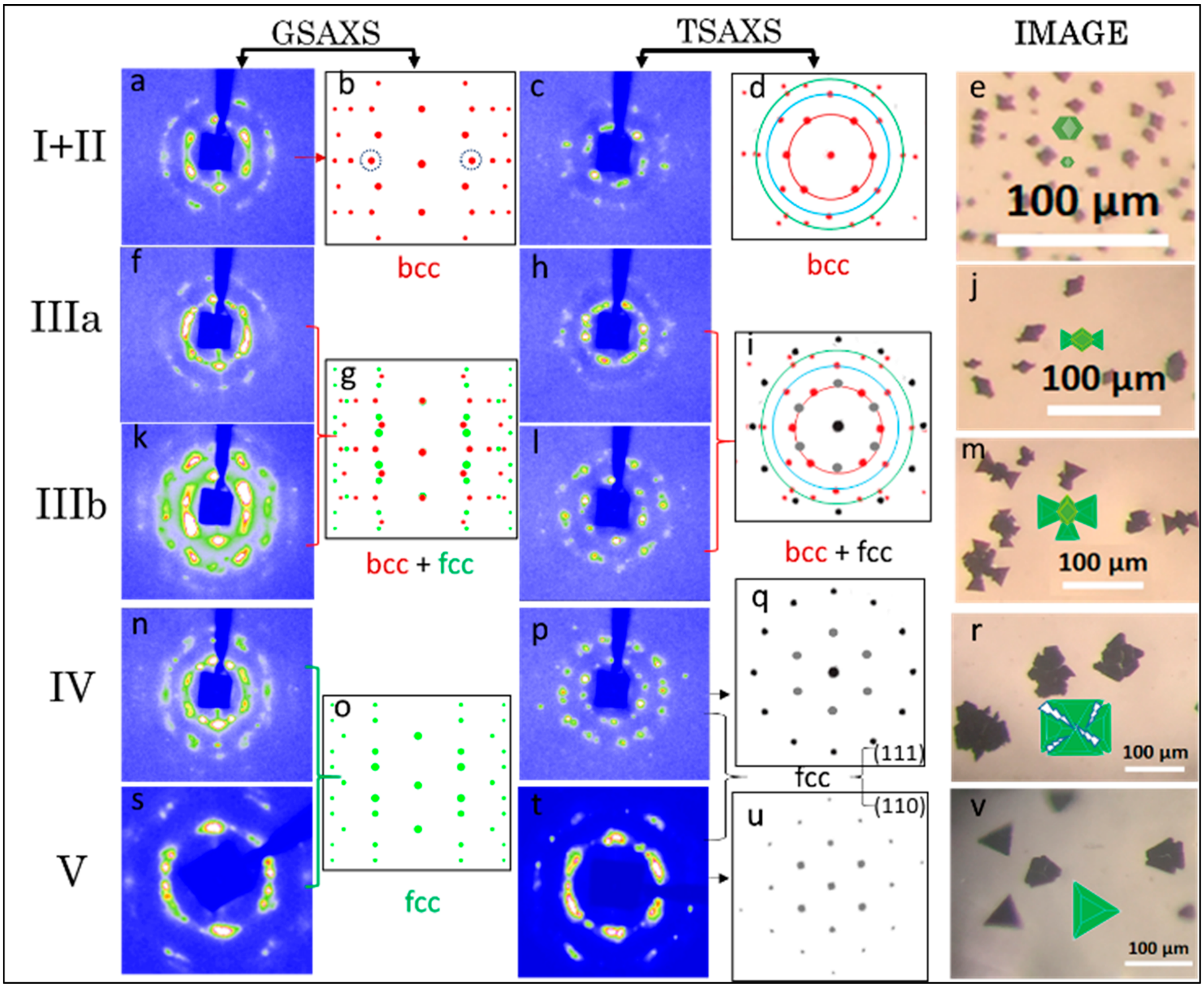

Figure 2. Structural and morphological characterizations of octahedral PbS NC supercrystals developed and attached at various locations of the glass capillary, indicative of the five key stages (I−V) from the starting antisolvent interface to the bottom of the capillary. GSAXS: (left) experimental and (right) simulated patterns with indexing, in which the spots circled in (b) are lacking in (a) because of the development of a preferred crystalline orientation. TSAXS: (left) experimental and (right) simulated patterns with indexing, in which (t) and (u) are not X-rays normal to fcc(111) plane, indeed close to fcc(110) due to the concave bottom of the capillary. Image: optical images and insets in green, highlighting the key features of the formed supercrystals at the corresponding stages. Note that indexing and analysis are given in Supporting Information, and the details can be seen in Figures S5−S9.

the supercrystal structures. In addition, careful examination of supercrystals under optical microscopy was made across the capillary from the antisolvent interface to the bottom, aiming to characterize the variations of supercrystals in grain size and morphology.

Figure 2 presents typical experimental and computational patterns of GSAXS and TSAXS and optical images of NC supercrystals distributed across the capillary. The detailed indexing and structural analysis of GSAXS and TSAXS images can be found in Figures S5−S9. Both experimental and computational GSAXS patterns reveal a developing consequence of superlattice transformation from bcc to fcc through an intermediate coexistence of bcc and fcc across the capillary from the interface to the bottom. Both fcc and bcc grains display an out-of-plane orientational ordering, in which fcc(111) and bcc(110) orientations overlap and are normal to the capillary wall (Figure 2 GSAXS and Figure S5). In excellent consistence with the above superlattice identification (Figure S6), TSAXS with simulations and spotty indexing further reveal the ordering of in-plane orientations in both bcc and fcc grains and the development of ordered arrangements between supercrystal grains (Figure 2 TSAXS and Figures S7−S9). The bcc grains are dominated by six symmetrical bcc(110) Bragg spots separated by a rotating angle of 60° (Figures 2c,d and S7), indicative of a preferred alignment of bcc grains along one 3-fold symmetrical axis, while the fcc grains manifest additional fcc(111) diffuse scattering spots, which are forbidden from scattering in the fcc(111) orientation normal to the incident X-rays (Figures 2q and S8), indicative of an apparent development of crystalline mosaicity within individual fcc grains. In an alignment with the structural development as described above, additional optical images correspondingly characterize the development of supercrystal grains in size from 1 to 100 μm and in morphology from rhombic to triangle shape (Figure 2 image and Figure S10). Associated with the above major changes of grain size and shape, there is apparently an intermediate region, where the supercrystals are developed with a typical butterfly-like bowtie structure stacked by three grains with a sandwich sequence of triangle−rhombus−triangle (Figure 2j,m), and the structures are characterized as a coexistence of bcc and fcc phases (Figure 2f,k,j,h,l,i and Figures S6b and S9). Combination and correlation of all these observed supercrystal structures and grain sizes as well as shapes as documented in Figure 2 allow one to identify the five key stages over the course of the supercrystal nucleation and growth process.

To make a direct connection of the observed superlattice transformation and morphological variation with the diffusion-mediated NC assembly process under a confined antisolvent environment, we carefully analyze the change of antisolvent diffusion rate as a function of time and then correlate such changes with the five identified stages toward improving our understanding on the antisolvent diffusion-mediated nucleation and growth of supercrystals and underlying mechanism. Utilizing the sharp interface formed by the dark NC suspended toluene and the overlying transparent ethanol (Figure S4), we are able to identify the time-dependent interface movement with subsequent determination of the antisolvent diffusion rate. Figure 3a shows the plot of the diffusion distance of ethanol across the soft and sharp interface into NC-suspended toluene as a function of time (min), highlighting the time-dependent variation of antisolvent diffusion rate. Obviously, the diffusion rates are not constant, so the diffusion-mediated process of NC assembly across the whole range of 31 mm within the glass capillary can be reasonably classified into the five key stages (I−V), consistent with these as identified and shown in Figure 2. Using the starting interface as a reference, a plot of grain size as a function of distance in Figure 3b further reveals the dependence of grain size on the time-dependent diffusion rate of antisolvents.

Obviously, the supercrystals grow fast at the early stages of I−II, and then the growth rate decreases slightly at stage III. At the final two stages of IV−V, the supercrystal growth behaves dramatically different, displaying a rapid jump of grain size at stage IV, and then a noticeable but unexpected reduction of grain size appears at stage V. At the first glimpse, it is difficult to find any obvious clues to make a feasible correlation between the observed antisolvent diffusion rates and the identified size distributions of supercrystal grains. Once all these data sets are connected with the observed variations of supercrystal shape and superlattice transformation over the course of the diffusion-mediated NC assembly process (Figures 2, 3, and 4), we are able to uncover a series of hidden linkages of the supercrystal nucleation and growth across the five identified stages for understanding the underlying mechanisms (Figure 4).

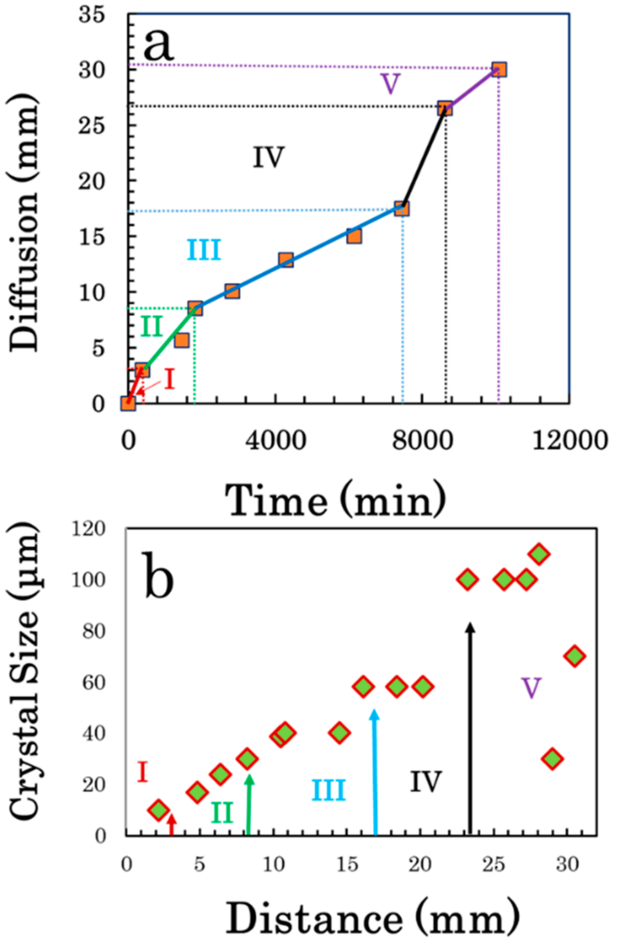

Figure 3. Antisolvent diffusion rates and diffusion-mediated nucleation and growth of octahedral PbS NC supercrystals: (a) variation of the diffusion distance of ethanol across the sharp interface into NC-suspended toluene as a function of time (min); (b) variation of the supercrystal grain size as a function of diffusion distance from the sharp interface to the bottom of the glass capillary.

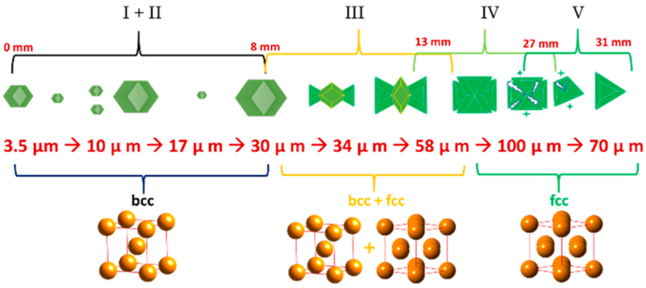

Figure 4. Schematic summary of the key features across the five stages of the nucleation and growth of octahedral PbS NC assembly, including the changes of the size and shape and structure of supercrystals.

As starting from the first stage (I), ethanol and toluene forms a sharp interface (Figure S4, left) and a large gradient between the two types of solvents is accordingly developed, which drives a quick diffusion of ethanol into toluene and thus triggers a burst crystallization of small supercrystal seeds. Such small seeds crystallize in a bcc structure and fall into a size distribution range of 1−3.5 μm in diameter (Figure 2a-d and Figures S6a and S10a). As the diffusion range expands wide and the diffusion rate reduces slightly, supercrystal growth continues and enters the second stage (II), the grains are developed with size distributions into the two typical ranges centered at 5 and 10 μm (Figure S11a), where the grain size of 10 μm is defined as a critical size due to its relatively enhanced structural stability. Meanwhile, an apparent Ostwald ripening effect (i.e., size-focusing) comes into play so that the supercrystal grains larger than the critical size of 10 μm continue to grow at the cost of smaller ones dissolving in solvents (Figure S10b−d). Upon growth of supercrystals with a grain size as large as 30 μm on average (Figure S10d,e), the supercrystal grains become homogeneous (Figure S11b), where individual grains display an ideal bcc(110)-terminated rhombic morphology.

Once getting into the stage of IIIa, the diffusion rate decreases slightly, and the symmetrical pairs of triangle crystals start nucleation and growth on the two symmetrical tips of individual rhombic crystals (Figures 2j and S10d). Accordingly, a typical butterfly-like bowtie structure is gradually developed. The triangle wings crystallize in a fcc structure (Figure 2f,g,h,i; Figures 4 and S6b), while the rhombus cores sandwiched between the two triangle wings still remain in a bcc structure. As the antisolvents continue diffusion at a nearly constant rate at stage IIIb (Figure 2k,g,l,I,m), the rhombus cores reduce in size until a complete disappearance. Simultaneously, the triangle wings grow larger and eventually touch directly. Occasionally, such crystals aggregate together and the shapes become slightly irregular. Randomly, additional triangle crystals appear on other rhombus tips (Figure 2m).

At stage IV, the diffusion rate increases dramatically, and two or three triangle pairs aggregate and start an oriented attachment process (Figure 2n,o,p,g,r and Figure 4). Such aggregated grains reach an average domain size of ∼100 μm (Figure 2r), and the developed interfaces within such individual aggregated grains display a weak and noticeable NC-dissolving feature, accordingly promoting effective development of preferred crystallographic orientation and NC rearrangement through interface and grain boundary (Figure 4).

At the final stage (V), the diffusion slows down again and has a diffusion rate close to that observed at stage III (Figure 2s,o,t,u,v and Figures 3a and 4). NC interactions through interface and boundary are dramatically enhanced, and the free-standing triangle crystals with a single fcc phase are developed by a spontaneous process of oriented attachment and enhanced NC rearrangement (Figure 2v, Figure S6c, and Figure 4). Upon elimination of the interface gap within aggregated grains, the single triangle crystals reduce in size from 100 to 70 μm (Figures 2v, 3b, 4), on average. However, the weak interface feature is still occasionally noticed (Figure 2v), evidently confirming the occurrence of preferred crystallographic orientation and attachment between supercrystal grains.

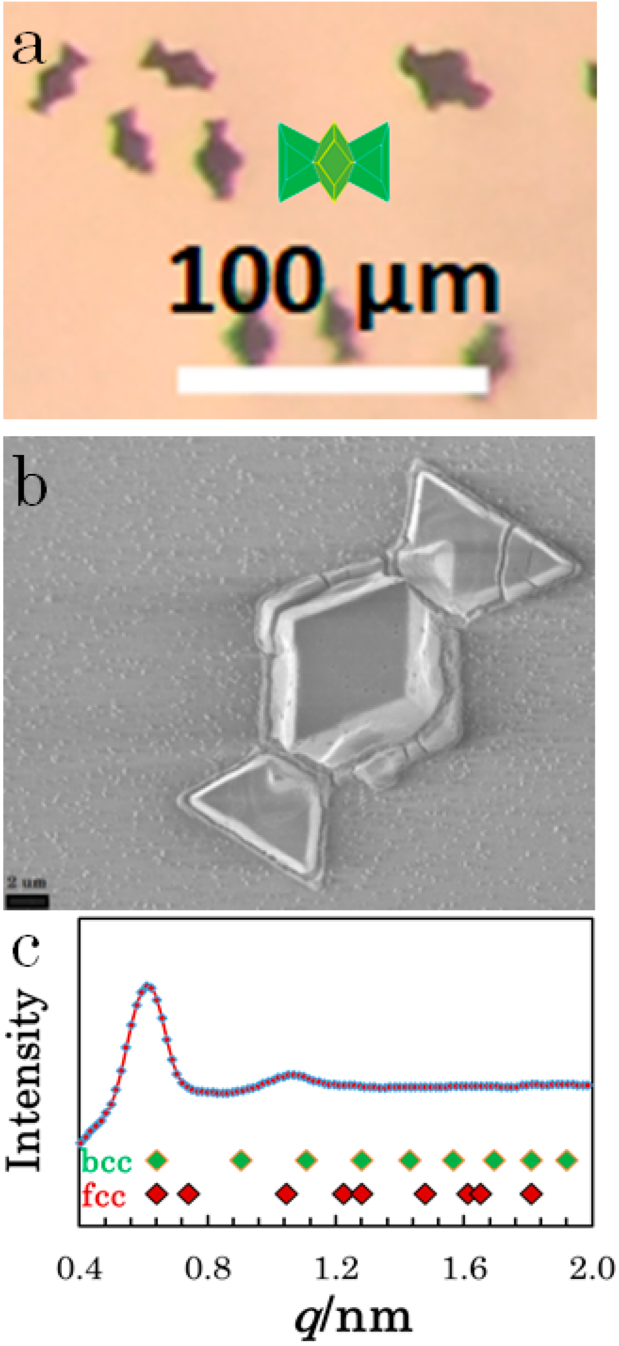

Figure 5. Highlights of individual butterfly-like bowtie supercrystals: (a) low-resolution optical image; (b) higher resolution SEM image; (c) 2D SAXS pattern with indexing of structures in fcc and bcc, respectively. Note that the long air-exposed and dried supercrystal displays multiple cracks, caused by an interplay between substrate-induced attraction and drying-induced superlattice contraction.

The butterfly-like bowtie stacking structure represents a significant intermediate phase, which is developed at the intermediate stage (III) and plays a connecting role in the formation of single free-standing phases from bcc and fcc superlattice. Figure 5 highlights the overall stacking structure of such typical butterfly-like bowtie supercrystals for additional analysis and mechanistic discussions. As shown in Figure 5a,b, each butterfly-like bowtie supercrystal is composed of the two fcc triangle wings and one bcc rhombus core, which is identified as a mixture of fcc and bcc (Figure 5c). Unlike the oriented attachment, the triangle crystals indeed originate from a secondary nucleation and growth of fcc superlattice directly on the tips of the bcc rhombus that have a higher surface energy as compared to the flat crystal facets, based on the classical crystal growth theory.[35] This seed-based nucleation and growth of triangle fcc supercrystals on the high-energy tips of the bcc rhombus not only dramatically reduce the overall surface energy of the early grown individual bcc grains but also apparently eliminate a fraction of surface area of the secondary nucleated individual fcc grains to avoid a full surface exposure to the surrounding environments. If bcc and fcc grains are treated as the two independent objects, this typical stacking structure allows bcc and fcc to help each other reduce surface energy of individual grains. Thermodynamically, such an attachment-resultant minimization of free energy enables improvement of the structure stability of supercrystals.

Obviously, the observed superlattice transformation in 3D supercrystals is different in underlying mechanism from 2D NC assembly.[26,36] As for the fcc-to-bcc superlattice transformation observed in 2D NC assembly, one study indicates that the superlattice transformation originates from a consequence of the primary melting (amorphization) of the early nucleated fcc at the interface and subsequent nucleation of bcc from such high density interface-mediated NC liquid,[26] while another study reveals that the superlattice transformation comes from a deformation-driven superlattice distortion, which follows the well-known Bain transformation pathway.[36] Differently, this diffusion-mediated 3D NC assembly study reveals a reversed bcc-to-fcc superlattice transformation over the course of the supercrystal nucleation and growth. Strictly speaking, this bcc-to-fcc superlattice transformation cannot be considered as one traditionally defined phase transition,[37−39] which normally involves the movement and rearrangement of building blocks (e.g., atoms and colloidal NCs) within individual crystals.[37−39] Instead, it is only a seed-based nucleation of secondary fcc directly on the early nucleated bcc seed crystals. In addition, the identification of the butterfly-bowties structure also allows one to unambiguously exclude the possibility of an oriented attachment driven mechanism of supercrystal growth (Figure 5a,b).

Based on various experimental observations and an overall analysis as well as reasonable correlations, we are able to reconstruct the pathway of the diffusion-mediated nucleation and growth of 3D supercrystals and even further to look at the driving mechanism behind (Figure 6). At the very early stage, the large gradient of antisolvents across the sharp interface drives a fast diffusion of ethanol into NC suspended toluene. Accordingly, NCs reduce their solubility in antisolvents and simultaneously increase NC concentration to accelerate the process of NC saturation in solvents. Such a quick NC saturation at the interface region triggers the burst nucleation and growth of a large number of rhombic supercrystals in a bcc structure but with large size distributions. Upon reduction of antisolvent gradient and continuous diffusion at a reduced rate, the supercrystal grains, which are larger than a critical size of 10 μm, continue to grow, whereas the smaller grains (<10 μm) become unstable and gradually dissolve into solvents. Once the supercrystal grains grow larger and approach 30 μm, a reduced diffusion rate appears to slow down the increasing rates of both NC concentration and NC saturation in solvents, and accordingly, the triangle fcc crystals start a seed-based secondary nucleation at the high energy tips of the bcc rhombus and thus develop into a series of butterfly-like bowtie structured supercrystals. As this typical intermediate process continues, the triangle wings grow larger, whereas the rhombus cores turn smaller. Upon complete dissolving of the rhombic cores, the triangle wings touch together to form a series of triangle pairs, which have a single fcc structure. A complex process takes place at the final two stages of IV and V, which are located at the capillary bottom (Figure 6, right) so that an oriented attachment process comes into play, and involves various degrees of NC dissolving and crystallographic rearrangement through multiple NC interactions at the interface and boundary of supercrystal grains.

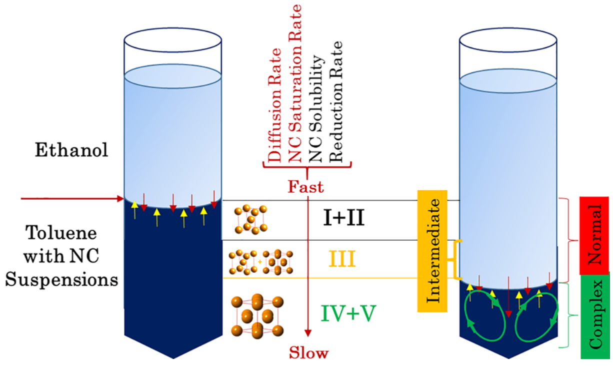

Figure 6. Demonstration of antisolvent diffusion process and associated interactions and resultant NC assembly. Note that arrows in red and orange indicate the gradient-driven normal antisolvent diffusions, and circles in green highlight the curvature induced convection flow at the capillary bottom.

Unlike the single play by the gradient driven antisolvent diffusion in the vertical direction dominated at the early three stages (I−III), the complex interactions occurring at stages IV−V involve a competition between the gradient driven normal antisolvent diffusion and the glass curvature-induced solvent convection (Figure 6, right), which induces a sudden change of antisolvent diffusion rate and subsequently causes the formation of the freestanding triangle single fcc supercrystals through a complicated consequence of supercrystal aggregation, oriented attachment, and NC rearrangement. However, it still remains largely unclear of how various driving forces change with solvent diffusion mediation and interact with environments to increase the complexity as observed at stages IV and V, thus making an impact on the nucleation and growth of NC supercrystals.

Additional studies are required to explore and understand such an increased complexity, but our study on the diffusion-mediated 3D supercrystal nucleation and growth certainly provides insights for designable control of NC assembly into large single supercrystals with desired superlattices. As an example, we designed and fabricated another capillary-based NC assembly cell, in which an air separation is intentionally confined in-between ethanol and toluene to reduce the antisolvent diffusion rate (Figure S12). With implementing control to weaken the liquid convection effect by horizontally placing the capillary on a static stage, the low NC concentration and slow NC saturation rate achieved by such a NC assembly design allow for our successful nucleation and growth of 3D free-standing fcc supercrystals that are rarely observed in previous 3D assembles of octahedral NCs.[26−29] As shown in Figure 7, the harvested supercrystals display a 3D freestanding triangle shape and have a narrow size distribution (Figure 7a,b). High resolution TEM characterization with a fast Fourier transform (fft) pattern reveals the single crystallinity of individual triangle supercrystals (Figure 7c), whereas GSAXS and TSAXS and 2D SAXS (Figure 7e,f) consistently confirm the single fcc phase. With such a control experiment and successful collection of target 3D fcc supercrystals, it is concluded that our diffusion-mediated NC assembly experimental study truly provides designing parameters (or principles) capable of controlled fabrication of 3D supercrystals with large scale and desired superlattices.

■ CONCLUSIONS

The diffusion-mediated experiments of octahedral PbS NC assembly were designed and performed to explore and understand as well as reconstruct the nucleation and growth pathway of large 3D free-standing supercrystals with various superlattices. As the diffusion of ethanol into NC-suspended toluene starts, a fast diffusion of antisolvents dramatically reduces NC solubility, where a quick increase of NC concentration appears to trigger a burst nucleation and growth of rhombic supercrystals that have a single bcc structure. At a critical size of 10 μm, a reduced diffusion rate and resultant

]

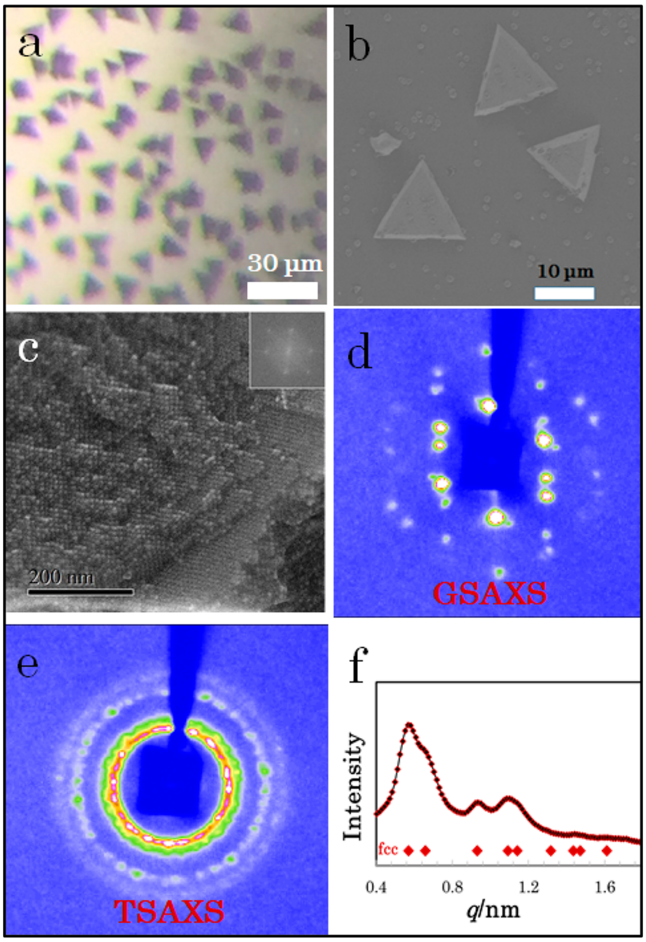

Figure 7. Controlled growth of free-standing 3D NC supercrystals with a single fcc structure controlled at a slow diffusion rate of antisolvents through placement of an air separation gap between ethanol and toluene: (a) low-resolution optical image; (b) SEM image; (c) high resolution TEM image with inset fft pattern; (d) GSAXS; (e) TSAXS; (f) 2D plot of TSAXS of collected triangle supercrystals.

lower NC concentration promote an Oswald ripening growth of large grains at cost of small grains dissolving in solvents. At a grain size of 30 μm, the diffusion process starts to activate the seed-based secondary nucleation and growth of the fcc triangle supercrystals on the tips of the bcc rhombus to form a butterfly-like bowtie structure. At a nearly constant diffusion rate, the triangle wings grow larger and are accordingly developed into a series of free-standing triangle pairs, while the rhombic cores reduce in size and disappear eventually. At the final stage, complex interactions appear to dramatically change the diffusion rate, and accordingly an oriented attachment event takes place to effectively promote the formation of free-standing triangle supercrystals with a single fcc phase. With experimental observations and collected insights, a novel NC assembly cell was designed and fabricated, where an air separation was intentionally tracked in-between antisolvents to reduce the diffusion rate of ethanol into NC-suspended toluene. Upon additional weakening of the complex interaction effect, the slow increase of NC concentration and spontaneous resultant NC saturation at a reduced rate drive the growth of large free-standing 3D supercrystals with a single fcc phase. Upon achievement of controlled growth of such desired 3D fcc supercrystals, this systematic work of diffusion-mediated NC assembly certainly provides designing principles for controlled fabrication of large 3D supercrystals with desired superlattices, capable of additional engineering of such supercrystals into new generation materials for research innovation and scientific discovery.

■ ASSOCIATED CONTENT

Supporting Information

The Supporting Information is available free of charge at https://pubs.acs.org/doi/10.1021/jacs.2c11120.

Additional data sets that include experimental and simulation details, figures, images, calculations, and analysis as well as indexing of TSAXS and GSAXS patterns (PDF)

■ AUTHOR INFORMATION

Corresponding Author

Zhongwu Wang − *Cornell High Energy Synchrotron Source, Cornell University, Ithaca, New York 14853, United States;* orcid.org/0000-0001-9742-5213; Email: zw42@cornell.edu

Authors

Xin Huang − *Cornell High Energy Synchrotron Source, Cornell University, Ithaca, New York 14853, United States;* orcid.org/0000-0001-5404-4437
Elizabeth Suit − *Cornell High Energy Synchrotron Source, Cornell University, Ithaca, New York 14853, United States;* orcid.org/0000-0001-7374-9029
Jinlong Zhu − *Department of Physics, South University of Science and Technology, Shenzhen, Guangdong 518055, China;* orcid.org/0000-0002-7314-8394
Binghui Ge − *Key Laboratory of Structure and Functional Regulation of Hybrid Materials of Ministry of Education, Institutes of Physical Science and Information Technology, Anhui University, Hefei, Anhui 230601, China*
Frauke Gerdes − *Institute of Physical Chemistry, University of Hamburg, 20146 Hamburg, Germany*
Christian Klinke − *Institute of Physics, University of Rostock, 18059 Rostock, Germany; Department of Chemistry, Swansea University—Singleton Park, Swansea SA2 8PP, U.K.;* orcid.org/0000-0001-8558-7389

Complete contact information is available at: https://pubs.acs.org/10.1021/jacs.2c11120

Notes

The authors declare no competing financial interest.

■ ACKNOWLEDGMENTS

We are grateful to many colleagues within CHESS and across the Cornell campus for technical assistance and scientific discussion. We appreciate that Dr. Zewei Quan helped take some optical and SEM images. The CHEXS is supported by the NSF Awards DMR-1332208 and DMR-1829070. This work also made use of the Cornell Center for Materials Research Shared Facilities, which is supported through the NSF MRSEC program (Grant DMR-1719875).

■ REFERENCES

(1) Boles, M. A.; Engel, M.; Talapin, D. V. Self-assembly of colloidal nanocrystals: from intricate structures to functional materials. *Chem. Rev.* **2016**, *116*, 11220−11289.

(2) Deng, K.; Luo, Z.; Tan, L.; Quan, Z. Self-assembly of anisotropic nanoparticles into functional superstructures. *Chem. Soc. Rev.* **2020**, *49*, 6002−6038.

(3) Henzie, J.; Grunwald, M.; Widmer-Cooper, A.; Geissler, P. L.; Yang, P. Self-assembly of uniform polyhedral silver nanocrystals into densest packings and exotic superlattices. *Nat. Mater.* **2012**, *11*, 131−137.

(4) Wang, T.; Zhuang, J.; Lynch, J.; Chen, O.; Wang, Z.; Wang, X.; Lamontagne, D.; Wu, H.; Wang, Z.; Cao, Y. C. Self-assembled Colloidal superparticles from nanorods. *Science* **2012**, *338*, 358−363.

(5) Raino, G.; Utzat, H.; Bawendi, M. G.; Kovalenko, M. V. Superradiant emission from self-assembled light emitters: from molecules to quantum dots. *MRS Bull.* **2020**, *45*, 841−848.

(6) Wu, H.; Bai, F.; Sun, Z.; Haddad; Boye, D. M.; Wang, Z.; Huang, J. Y.; Fan, H. Nanostructured gold architectures formed through high pressure-driven sintering of spherical nanoparticle arrays. *J. Am. Chem. Soc.* **2010**, *132*, 12826−12828.

(7) Zhu, H.; Nagaoka, Y.; Hills-Kimball, K.; Tan, J.; Yu, L.; Fang, Y.; Wang, K.; Li, R.; Wang, Z.; Chen, O. Pressure-enabled synthesis of hetero-dimers and hetero-rods through intrapaticle coalescence and interparticle fusion of quantum-dot-Au satellite nanocrystals. *J. Am. Chem. Soc.* **2017**, *139*, 8408−8411.

(8) Huang, X.; Wang, Z. Supercrystallography-based decoding of structure and driving force of nanocrystal assembly. *Materials* **2019**, *12* (22), 3771.

(9) Bai, F.; Bian, K.; Huang, X.; Wang, Z.; Fan, H. Pressure induced nanoparticle phase behavior, property and applications. *Chem. Rev.* **2019**, *119*, 7673−7717.

(10) Xiao, T.; Nagaoka, Y.; Wang, X.; Jiang, T.; LaMontagne, D.; Zhang, Q.; Cao, C.; Diao, X.; Qiu, J.; Lu, Y.; Wang, Z.; Cao, Y. C. Nanocrystal with metastable high-pressure phases under ambient conditions. *Science* **2022**, *377*, 870−874.

(11) Park, D. J.; Zhang, C.; Ku, J. C.; Zhou, Y.; Schatz, G. C.; Mirkin, C. A. Plasmonic photonic crystals realized through DNA-programmable assembly. *Proc. Natl. Acad. Sci. U.S.A.* **2015**, *112*, 977−981.

(12) Park, D. J.; Ku, J. C.; Sun, L.; Lethiec, C. M.; Stern, N.; Schatz, G. C.; Mirkin, C. A. Directional emission from dye-functionalized plasmonic DNA superlattice microcavities. *Proc. Natl. Acad. Sci. U.S.A.* **2017**, *114*, 457−461.

(13) Bian, K.; Schunk, H.; Ye, D.; Hwang, A.; Luk, T. S.; Li, R.; Wang, Z.; Fan, H. Formation of self-assembled gold nanoparticle supercrystals with facet-dependent surface plasmonic coupling. *Nat. Commun.* **2018**, *9*, 2365.

(14) Deng, K.; Huang, X.; Liu, Y.; Xu, L.; Li, R.; Tang, J.; Lei, Q.; Ni, R.; Li, C.; Zhao, Y. S.; Xu, H.; Wang, Z.; Quan, Z. Supercrystallographic reconstruction of 3D nanorod assembly with collectively anisotropic upconversion fluorescence. *Nano Lett.* **2020**, *20*, 7367−7374.

(15) LaMer, V. K.; Dinegar, R. H. Theory, production and mechanism of formation of monodispersed hydrosols. *J. Am. Chem. Soc.* **1950**, *72*, 4847−4854.

(16) Toschev, S. Homogeneous nucleation. In *Crystal Growth: An Introduction Homogeneous Nucleation*; Hartman, P., Ed.; Elsevier: New York, 1973; pp 1−49.

(17) Cushing, B. L.; Kolesnichenko, V. L.; O'Connor, C. J. Recent advances in the liquid-phase syntheses of inorganic nanoparticles. *Chem. Rev.* **2004**, *104*, 3893−3946.

(18) Ostwald, W. Studien uber die Bildung und Umwandlung fester Korper. 1. Abhandlung: Ubersattigung und Uberkaltung. *Z. Phys. Chem.* **1897**, *22U*, 289.

(19) Penn, R. L.; Banfield, J. F. Imperfect oriented attachment: dislocation generation in defect-free nanocrystals. *Science* **1998**, *281*, 969−971.

(20) Li, D.; et al. Direction-specific interactions control crystal growth by oriented attachment. *Science* **2012**, *336*, 1014−1018.

(21) Zhang, H.; De Yoreo, J. J.; Banfield, J. F. A unified description of attachment-based crystal growth. *ACS Nano* **2014**, *8*, 6526−6530.

(22) De Yoreo, J. J.; et al. Crystallization by particle attachment in synthetic, biogenic and geologic environments. *Science* **2015**, *349*, aaa6760.

(23) Mirabello, G.; Ianiro, A.; Bomans, P. H. H.; Yoda, T.; Arakaki, A.; Friedrich, H.; de With, G.; Sommerdijk, N. A. J. M. Crystallization by particle attachment is a colloidal assembly process. *Nat. Mater.* **2020**, *19*, 391−396.

(24) Wang, F.; Richards, V. N.; Shields, S. P.; Buhro, W. E. Kinetics and Mechanisms of Aggregative Nanocrystal Growth. *Chem. Mater.* **2014**, *26*, 5−21.

(25) Wang, Z.; Bian, K.; Nagaoka, Y.; Fan, H.; Cao, Y. C. Regulating multiple variables to understand the nucleation and growth and transformation of PbS nanocrystal superlattices. *J. Am. Chem. Soc.* **2017**, *139*, 14476−14482.

(26) Huang, X.; Zhu, J.; Ge, B.; Gerdes, F.; Klinke, C.; Wang, Z. In situ constructing the kinetic roadmap of octahedral nanocrystal assembly toward controlled superlattice fabrication. *J. Am. Chem. Soc.* **2021**, *143*, 4234−4243.

(27) Li, R.; Zhang, J.; Tan, R.; Gerdes, F.; Luo, Z.; Xu, H.; Hollingsworth, J. A.; Klinke, C.; Chen, O.; Wang, Z. Competing interactions between various entropic forces toward assembly Pt_3Ni octahedra into a body-centered cubic superlattice. *Nano Lett.* **2016**, *16*, 2792−2799.

(28) Zhang, J.; Luo, Z.; Quan, Z.; Wang, Y.; Kumbhar, A.; Smilgies, D. M.; Fang, J. Low packing density self-assembled superstructure of octahedral Pt3Ni nanocrystals. *Nano Lett.* **2011**, *11*, 2912−2918.

(29) Zhang, J.; Luo, Z.; Martens, B.; Quan, Z.; Kumbhar, A.; Porter, N.; Wang, Y.; Smilgies, D. M.; Fang, J. Reversible Kirkwood-Alder transition observed in Pt_3Cu_2 nanoctahedron assemblies under controlled solvent annealing/drying conditions. *J. Am. Chem. Soc.* **2012**, *134*, 14043−14049.

(30) Gerdes, F.; Volkmann, M.; Schliehe, C.; Bielewicz, T.; Klinke, C. Sculpting of lead sulfide nanoparticles by means of acetic acid and dichloromethane. *Z. Phys. Chem.* **2015**, *229*, 139−151.

(31) Pileni, M. P. Supracrystals of inorganic nanocrystals: an open challenge for new physical properties. Acc. *Chem. Res.* **2008**, *41*, 1799−1809.

(32) Cheng, C.; Wei, J.; Yang, Z. Shape-controlled self-assembly of truncated octahedral nanocrystals into supracrystals. *J. Phys. Chem. C* **2021**, *125*, 26942−26950.

(33) Ni, B.; Gonzalez-Rubio, G.; Colfen, H. Self-assembly of colloidal nanocrystals into 3D binary mesocrystals. *Acc. Chem. Res.* **2022**, *55*, 1599−1608.

(34) Schlotheuber né Brunner, J.; Maier, B.; Thomä, S. L. J.; Kirner, F.; Baburin, I. A.; Lapkin, D.; Rosenberg, R.; Sturm, S.; Assalauova, D.; Carnis, J.; Kim, Y. Y.; Ren, Z.; Westermeier, F.; Theiss, S.; Borrmann, H.; Polarz, S.; Eychmüller, A.; Lubk, A.; Vartanyants, I. A.; Cölfen, H.; Zobel, M.; Sturm, E. V. Morphogenesis of Magnetite Mesocrystals: Interplay between Nanoparticle Morphology and Solvation Shell. *Chem. Mater.* **2021**, 33, 9119−9130.

(35) Xia, Y.; Xiong, Y.; Lim, B.; Skrabalak, S. E. Shap-controlled synthesis of metal nanocrystals: simple chemistry meets complex physics? *Angew. Chemie. Int. Ed.* **2009**, *48*, 60−103.

(36) Weidman, M. C.; Smilgies, D. M.; Tisdale, W. A. Kinetics of the self-assembly of nanocrystal superlattice measured by real-time in situ x-ray scattering. *Nat. Mater.* **2016**, *15*, 775−781.

(37) Wang, Z.; Wen, X.-D.; Hoffmann, R.; Son, J. S.; Li, R.; Fang, C.-C.; Smilgies, D.-M.; Hyeon, T. Reconstructing a solid-solid phase transformation pathway in CdSe nanosheets with associated soft ligand. *Proc. Natl. Acad. Sci. U.S.A.* **2010**, *107*, 17119−17124.

(38) Huang, X.; Zhu, J.; Ge, B.; Deng, K.; Wu, X.; Xiao, T.; Jiang, T.; Quan, Z.; Cao, Y. C.; Wang, Z.; Fan, H. Understanding Fe_3O_4 Nanocube Assembly with Reconstruction of a Consistent Superlattice Phase Diagram. *J. Am. Chem. Soc.* **2019**, *141*, 3198−3206.

(39) Zhang, Y.; Lu, F.; Van Der Lelie, D.; Gang, O. Continuous phase transformation in nanocube assemblies. *Phys. Rev. Lett.* **2011**, *107*, 135701.